Optics & Laser Technology 163 (2023) 109400

Contents lists available at ScienceDirect

Optics and Laser Technology

journal homepage: www.elsevier.com/locate/optlastec

Full length article

Vector diffractive optical element as a full-Stokes analyzer

Angela Soria-Garcia [a,*], Jesus del Hoyo [a], Luis Miguel Sanchez-Brea [a], Veronica Pastor-Villarrubia [a,b], Veronica Gonzalez-Fernandez [b], Mahmoud H. Elshorbagy [c], Javier Alda [b]

[a] Applied Optics Complutense Group, Optics Department, Faculty of Physics, Universidad Complutense de Madrid, Plaza de las Ciencias 1, 28040, Madrid, Spain
[b] Applied Optics Complutense Group, Optics Department, Faculty of Optics and Optometry, Universidad Complutense de Madrid, C/ Arcos de Jalón 118, 28037, Madrid, Spain
[c] Faculty of Science, Minia University, 61519 El-Minya, Egypt

ARTICLE INFO

Keywords:
Polarimetry
Diffractive optics
Vector Diffractive Optical Elements
Stokes parameters

ABSTRACT

The real-time characterization of the polarization state of a light beam is of importance for a variety of applications in Optics and Photonics. We have designed a device that includes a Vector Diffractive Optical Element (VDOE) to determine the polarization state of an incident light beam. The device is able to simultaneously evaluate the four Stokes parameters of the light under analysis. The VDOE is sectorized into several Fresnel zone plates, enabling a compact arrangement and facilitating optoelectronical integration. We have also developed a procedure to remove diffractive effects and systematic errors. From the simulated results, our device is able to identify any polarization incident state with an averaged uncertainty of 0.006%. Finally, we have experimentally verified the VDOE with non-ideal polarization elements to further validate and test our proposed design. The averaged uncertainty of our experimental realization is 3.33%.

1. Introduction

The state of polarization of light – the orientation of the accompanying electric vector – is key to understand how electromagnetic radiation interacts with matter. From the simple evaluation of the energy budget at the interface of two different media, to the more complex analysis of the excitation of plasmonic resonances, polarization determines how light behaves and how it can be used for possible applications. In consequence, the polarization state of a light beam is a relevant parameter in many fields, such as material analysis, chemistry, medicine, defense, remote sensing, astrophysics, biology, etc. [1–3]. Mathematically, the polarization state of light can be described in two ways: the Jones vector (in the Jones formalism), which only deals with pure polarized states, and the Stokes vector (in the Mueller–Stokes formalism), which allows the characterization of any type of polarization state, where the Stokes vector interacts with elements described by Mueller matrices.

There are several techniques to determine the polarization state of a light beam [4]. One of the most popular methods consists of a rotating linear retarder, followed by a fixed linear polarizer [5,6]. The transmitted light is measured with a photodetector, which generates a signal dependent on the angle of the rotating linear retarder. From this signal, the Stokes vector of the incident field can be obtained. In order to eliminate moving parts, the retardance modulation can be performed with Pockels cells [7], liquid crystals [8], or photoelastic modulators [9]. Nevertheless, these sequential strategies are unable to measure simultaneously all the components of the Stokes vector. A real-time measurement is possible with division-of-amplitude polarimetric techniques which records the Stokes parameters at the same time. For example, in [10], the incoming light is divided into four beams by beam-splitters that, after crossing polarization components, reach four photodetectors that provide the signals to evaluate the four Stokes parameters. However, this procedure entails voluminous and expensive elements. Another division-of-amplitude solution is given in [11], where the beam under analysis is diffracted by two consecutive gratings, increasing the length of the assembly, or in [12], which divide the beam intensity unevenly. Some other designs use polarization-selective devices based on optical antennas and resonant optics [13,14]. For example, an appropriate combination of infrared antennas generates signals proportional to S_1, S_2, and S_3, using bolometric [15] or Seebeck [16] transduction mechanisms. Other recent approaches exploit the capability of nanometric resonant structures to induce retardance and modify the state of polarization of a given beam [17–19], generating new devices that efficiently measure the Stokes parameters [20–22].

* Corresponding author.
E-mail address: angsoria@ucm.es (A. Soria-Garcia).

https://doi.org/10.1016/j.optlastec.2023.109400
Received 23 December 2022; Received in revised form 25 February 2023; Accepted 17 March 2023
Available online 29 March 2023

In this paper, we utilize Diffractive Optical Elements (DOEs) combined with polarizers and retarders spatially distributed in sectors on the aperture of the DOE. This combination generates a device that modifies the vector characteristics of light crossing it, i.e., its polarization state. The modification follows the spatial distribution of the underlying DOE. This is why, we have named this element as a Vector Diffractive Optical Element (VDOE) as a natural evolution of the DOE concept. In this manuscript, the proposed VDOE is devoted to the characterization of the polarization state of an incoming beam. Classical DOEs comprise Fresnel zone plates, phase plates, beam shapers, computer generated holograms, kinoforms, and a wide variety of customized optical elements [23–26]. When necessary, light intensity and phase have been combined and redistributed using sectorized DOEs. For example, this strategy has been used to design extended depth of focus lenses (EDOF) and to generate vector beams [27–30]. DOEs usually modulate the amplitude or phase of the incident beam. However, they can also modulate the coherence [31–34] or the state of polarization. In this last case, a DOE becomes a VDOE. In our design, the entry aperture of the VDOE is angularly distributed in several sectors. Each sector takes the form of a Fresnel Zone Plate (FZP) where the vector character is given by an appropriate combination of a polarizer and, when necessary, a retardance plate. The light emerging from the VDOE is collected at the image plane of the VDOE, where a detection system is placed. The electric signals corresponding to each sector depend on the state of polarization of the incident beam. Once processed, we obtain the Stokes vector of the incident light beam as a combination of the signals obtained at the image plane. Our analysis also considers the systematic errors caused by diffraction and the non-ideal behavior of the VDOE's elements. Through this study, we have developed a method that includes these uncertainties and make the characterization of the state of polarization of light more robust, precise, and reliable.

The paper is organized as follows. In Section 2, we present the Stokes analyzer device based on a VDOE. We explain the working principle behind it and how the Stokes vector can be measured for ideal cases. In Section 3, we evaluate the device's performance with numerical simulations and estimate diffractive cross-talking and systematic errors and how to compensate them (e.g., the error for pure polarization states is numerically obtained). In Section 4, we describe the fabrication steps required to obtain a working VDOE, and how the device determines the Stokes vector of the incident beam experimentally. After removing the systematic errors, an averaged uncertainty of 3.33% remains. The sources of this discrepancy are analyzed and explained. Finally, Section 5 summarizes the main conclusions and findings of this contribution.

2. Design and modeling

Let us consider a light beam with a given polarization state defined by the Stokes vector [2]

$$\vec{S} = \begin{pmatrix} S_0 \\ S_1 \\ S_2 \\ S_3 \end{pmatrix} = \begin{pmatrix} I_T \\ I_{0^\circ} - I_{90^\circ} \\ I_{45^\circ} - I_{135^\circ} \\ I_{\mathrm{RCP}} - I_{\mathrm{LCP}} \end{pmatrix}, \tag{1}$$

where S_0 is the total intensity of the beam, S_1 is obtained subtracting the intensity of the vertical polarization component from the horizontal polarization component, S_2 makes the same with the intensities of the linear polarization at 45° and 135° (or −45°), and S_3 is the difference between the intensities of the left-circular polarization and the right-circular polarization components. Our objective is to measure the Stokes vector of this beam using a compact, fast, and simple device. For this, we utilize a sectorized VDOE where each sector is formed by a Vector Fresnel Zone Plate (VFZP) having the same focal length, f', for a given wavelength, λ, but de-centered with respect to the geometrical center of the VDOE by an amount Δr. The de-centering is necessary to spatially distinguish the contribution from each sector. This arrangement generates as many focal points as the number of sectors. Although the minimum number of sectors for the Stokes analyzer is 4, more sectors will reduce errors due to oversampling [6].

The distribution of the transmittance of the VDOE for N equally distributed angular sectors can be analytically expressed at each pth Fresnel zone ring as the following transmittance distribution, $T_{k,p}$, for each k sector

$$T_{k,p}(x,y) = 0.5\left[T_0\left(1+(-1)^p\right) + T_k\left(1+(-1)^{p-1}\right)\right], \tag{2}$$

where T_0 describes the obscured zones and T_k describes the open zones that are filled with the corresponding polarization elements. In fact, these transmittances should be considered as Jones or Mueller matrices. The parameter p runs from 1 to the maximum index of the last zone, P, included within the angular sector, k. Eq. (2) is valid for those locations (x, y) complying with conditions

$$(p-1)\lambda f' \le (x - \Delta r\cos\alpha_{k,c})^2 + (y - \Delta r\sin\alpha_{k,c})^2 < p\lambda f' \text{ , for } p = 1,\ldots,P, \tag{3}$$

where P is the total number of Fresnel zones, and

$$x^2 + y^2 \le R_T^2, \tag{4}$$

$$\alpha_{k,\min} \le \mathrm{atan}(y,x) < \alpha_{k,\max}. \tag{5}$$

In Eqs. (4) and (5), R_T is the radius of the total aperture of our VDOE, $\mathrm{atan}(x, y)$ is the two-argument $\tan^{-1}$ function, and $\alpha_{k,\min}$ and $\alpha_{k,\max}$ are the angular limits of each sector of the VDOE that are given as

$$\alpha_{k,\min} = \alpha_{k,c} - \frac{\pi}{N}, \tag{6}$$

$$\alpha_{k,\max} = \alpha_{k,c} + \frac{\pi}{N}. \tag{7}$$

The angle at the center of each sector, $\alpha_{k,c}$, in Eqs. (3), (6) and (7) is given as

$$\alpha_{k,c} = (2k+1)\frac{\pi}{N} + \alpha_0 \text{ , for } k = 1,\ldots,N, \tag{8}$$

where α_0 describes the origin of the distribution of sectors and it is typically set to zero.

For the simulations and device fabrication, we have selected a VDOE with 6 sectors which generate 6 focal points on the same focal plane, meaning that $N = 6$ in Eqs. (6) and (7). Fig. 1 shows an example of the sectorized VDOE. The device has a circular aperture with a diameter of $R_T = 6$ mm, and it is sectorized in equal angular regions. These regions are filled with VFZPs having the same focal distance, $f' = 200$ mm for the design wavelength of $\lambda = 0.6328\,\mu$m. The optical axis of each Fresnel lens is de-centered $\Delta r = 1.5$ mm from the center of the circular aperture of the VDOE. We consider this offset distance to limit the maximum number of Fresnel zones, so we avoid the presence of very narrow zones that could be reproduced with low resolution, both towards the VDOE center and the outer limit of the aperture. Each sector corresponds to one of the six polarization states associated with the intensities included in Eq. (1). As we will explain later, this configuration provides signals that are well adapted to the ideal case, simplifying the discussion of the results. The VDOE incorporates different polarization elements, shown with different colors in Fig. 1. The Jones and Mueller matrices for each element are described in Table 1. They are labeled with an integer number from 0 to 6, where 0 corresponds to null transmittance and 1–6 code the polarization elements. For the proposed design, we have used 4 polarizers with a linear transmission state oriented at 0°, 90°, 45°, 135° ($k = 1, 2, 3$, and 4), and 2 circular polarizers with right- and left-handed transmission states ($k = 5$ and 6).

We select the Stokes–Mueller formalism – the state of polarization of light is described by a Stokes vector and the system is given as a Mueller matrix – to describe the optical behavior of the proposed VDOE. In our first approach, we consider that the polarization elements

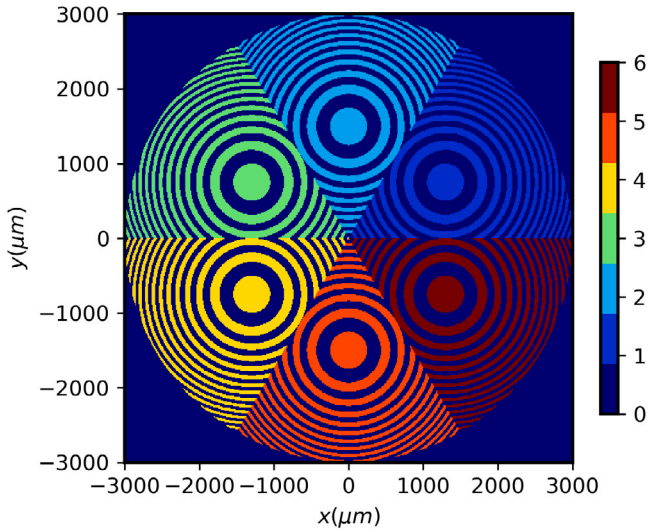

Fig. 1. Geometrical layout of the sectorized VDOE. Each color, labeled with an integer number $k = 0, \ldots, 6$, represents a different polarization matrix (described in Table 1), where $k = 0$ represents opaque zones.

Table 1
Jones and Mueller matrices for the different labeled portions in Fig. 1 in the ideal case where there is no depolarization. The label k also denotes the given sector of the VDOE as presented in Fig. 1.

k	Jones matrix	Mueller matrix
0	$\boldsymbol{J}_D = \begin{pmatrix} 0 & 0 \\ 0 & 0 \end{pmatrix}$	$\boldsymbol{M}_D = \begin{pmatrix} 0 & 0 & 0 & 0 \\ 0 & 0 & 0 & 0 \\ 0 & 0 & 0 & 0 \\ 0 & 0 & 0 & 0 \end{pmatrix}$
1	$\boldsymbol{J}_{0^\circ} = \begin{pmatrix} 1 & 0 \\ 0 & 0 \end{pmatrix}$	$\boldsymbol{M}_{0^\circ} = \frac{1}{2}\begin{pmatrix} 1 & 1 & 0 & 0 \\ 1 & 1 & 0 & 0 \\ 0 & 0 & 0 & 0 \\ 0 & 0 & 0 & 0 \end{pmatrix}$
2	$\boldsymbol{J}_{90^\circ} = \begin{pmatrix} 0 & 0 \\ 0 & 1 \end{pmatrix}$	$\boldsymbol{M}_{90^\circ} = \frac{1}{2}\begin{pmatrix} 1 & -1 & 0 & 0 \\ -1 & 1 & 0 & 0 \\ 0 & 0 & 0 & 0 \\ 0 & 0 & 0 & 0 \end{pmatrix}$
3	$\boldsymbol{J}_{45^\circ} = \frac{1}{2}\begin{pmatrix} 1 & 1 \\ 1 & 1 \end{pmatrix}$	$\boldsymbol{M}_{45^\circ} = \frac{1}{2}\begin{pmatrix} 1 & 0 & 1 & 0 \\ 0 & 0 & 0 & 0 \\ 1 & 0 & 1 & 0 \\ 0 & 0 & 0 & 0 \end{pmatrix}$
4	$\boldsymbol{J}_{135^\circ} = \frac{1}{2}\begin{pmatrix} 1 & -1 \\ -1 & 1 \end{pmatrix}$	$\boldsymbol{M}_{135^\circ} = \frac{1}{2}\begin{pmatrix} 1 & 0 & -1 & 0 \\ 0 & 0 & 0 & 0 \\ -1 & 0 & 1 & 0 \\ 0 & 0 & 0 & 0 \end{pmatrix}$
5	$\boldsymbol{J}_R = \frac{1}{2}\begin{pmatrix} 1 & -i \\ i & 1 \end{pmatrix}$	$\boldsymbol{M}_R = \frac{1}{2}\begin{pmatrix} 1 & 0 & 0 & 1 \\ 0 & 0 & 0 & 0 \\ 0 & 0 & 0 & 0 \\ 1 & 0 & 0 & 1 \end{pmatrix}$
6	$\boldsymbol{J}_L = \frac{1}{2}\begin{pmatrix} 1 & i \\ -i & 1 \end{pmatrix}$	$\boldsymbol{M}_L = \frac{1}{2}\begin{pmatrix} 1 & 0 & 0 & -1 \\ 0 & 0 & 0 & 0 \\ 0 & 0 & 0 & 0 \\ -1 & 0 & 0 & 1 \end{pmatrix}$

are ideal and do not depolarize the incoming light. In consequence, the transformation between Jones and Mueller representation is simple and bijective [35,36]. In Fig. 2, we represent the 16 elements $m_{jj'}$ (where $j, j' = 0, 1, 2, 3$) of the Mueller matrix as maps which reproduce the VDOE's geometry.

We obtain the intensity distribution at the image plane (or focal plane for a collimated input beam) by using the vector Rayleigh–Sommerfeld approach (VRS) [37]. We have implemented it with two open-source Python libraries: Diffractio for propagation of light, and

Table 2
Polarization states l of the simulated incident light beams.

l	1	2	3	4	5	6
Name	$\vec{S}^{\text{in}}_{0^\circ}$	$\vec{S}^{\text{in}}_{90^\circ}$	$\vec{S}^{\text{in}}_{45^\circ}$	$\vec{S}^{\text{in}}_{135^\circ}$	$\vec{S}^{\text{in}}_{R}$	$\vec{S}^{\text{in}}_{L}$
Stokes	$\begin{pmatrix} 1 \\ 1 \\ 0 \\ 0 \end{pmatrix}$	$\begin{pmatrix} 1 \\ -1 \\ 0 \\ 0 \end{pmatrix}$	$\begin{pmatrix} 1 \\ 0 \\ 1 \\ 0 \end{pmatrix}$	$\begin{pmatrix} 1 \\ 0 \\ -1 \\ 0 \end{pmatrix}$	$\begin{pmatrix} 1 \\ 0 \\ 0 \\ 1 \end{pmatrix}$	$\begin{pmatrix} 1 \\ 0 \\ 0 \\ -1 \end{pmatrix}$

Py-pol for polarization analysis [38,39]. Our simulations consider a spatial sampling of 1024 × 1024 points for those planes perpendicular to the optical axis. The result of this computation is the electric field at the focal plane of the VDOE: $\vec{E}(x, y) = \begin{bmatrix} E_x(x, y), & E_y(x, y), & E_z(x, y) \end{bmatrix}^T$, where ^{T} means transpose. In our analysis, we have neglected the axial component of the field $E_z(x, y)$ because the proposed VDOE presents a large numerical aperture with $F\# = 33.3$, valid in paraxial approximation.

Assuming a collimated beam, we have numerically evaluated the intensity distribution at the focal plane, $I(x, y) = \left|\vec{E}(x, y)\right|^2$, for the 6 incident polarization states described in Table 2. These input polarization states are linearly polarized at 0°, 90°, 45°, and 135° for $l = 1, 2, 3$ and 4, respectively, and right- and left-circularly polarized for $l = 5$ and $l = 6$. We have selected these 6 states to produce a null transmission in one of the sectors of the VDOE. The intensity distributions at the focal plane for these 6 polarization states are shown in Fig. 3 (upper row). The light intensities reaching the six focii, I_k, are detected by six photodetectors placed on the focal plane of the sectorized VDOE. With this setup, the polarization of the incoming light beam can be determined from signals I_k. When the polarization matrices correspond to those of Table 1, the Stokes vectors $\vec{S}^{\text{sim}}_l$ are

$$\vec{S}^{\text{sim}}_l = \begin{pmatrix} S^{\text{sim}}_{0,l} \\ S^{\text{sim}}_{1,l} \\ S^{\text{sim}}_{2,l} \\ S^{\text{sim}}_{3,l} \end{pmatrix} = \begin{pmatrix} \frac{1}{3}\sum_{k=1}^{6} I_{k,l} \\ I_{1,l} - I_{2,l} \\ I_{3,l} - I_{4,l} \\ I_{5,l} - I_{6,l} \end{pmatrix}, \tag{9}$$

where the superindex $^{\text{sim}}$ means that the Stokes parameters are obtained through simulation. The intensities $I_{k,l}$ are given by the detector k (corresponding to the VDOE's sector k) and by the input radiation with a polarization state l presented in Table 2.

So far, we have seen how ideal elements perform. However, the input Stokes vector must be determined differently when the polarization matrices are different from those in Table 1 [6]. Let us consider that the Mueller matrix associated to sector k is $\boldsymbol{M}_k$. Then, the intensity that passes through the k^{th} sector is

$$I_k = \sum_{j=0}^{3} m_{0j,k} S^{\text{in}}_j. \tag{10}$$

From Eq. (10), we see that the intensity I_k depends only on the first row of $\boldsymbol{M}_k$.

To generalize the design of a working VDOE for full-Stokes characterization, we can define N as the number of sectors in a given device, knowing that $N \geq 4$. Therefore, all the intensities I_k can be included in a N-component vector $\vec{I}$, so that (10) is described as

$$\vec{I} = \boldsymbol{W}\vec{S}^{\text{in}}, \tag{11}$$

where $\boldsymbol{W}$ is a $N \times 4$ matrix. In consequence, the Stokes vector can be calculated as

$$\vec{S}^{\text{in}} = \boldsymbol{W}^I \vec{I}, \tag{12}$$

where $\boldsymbol{W}^I = \boldsymbol{W}^{-1}$ for $N = 4$. When $N > 4$, $\boldsymbol{W}^I$ is the pseudoinverse matrix, defined as

$$\boldsymbol{W}^I = (\boldsymbol{W}^T\boldsymbol{W})^{-1}\boldsymbol{W}^T. \tag{13}$$

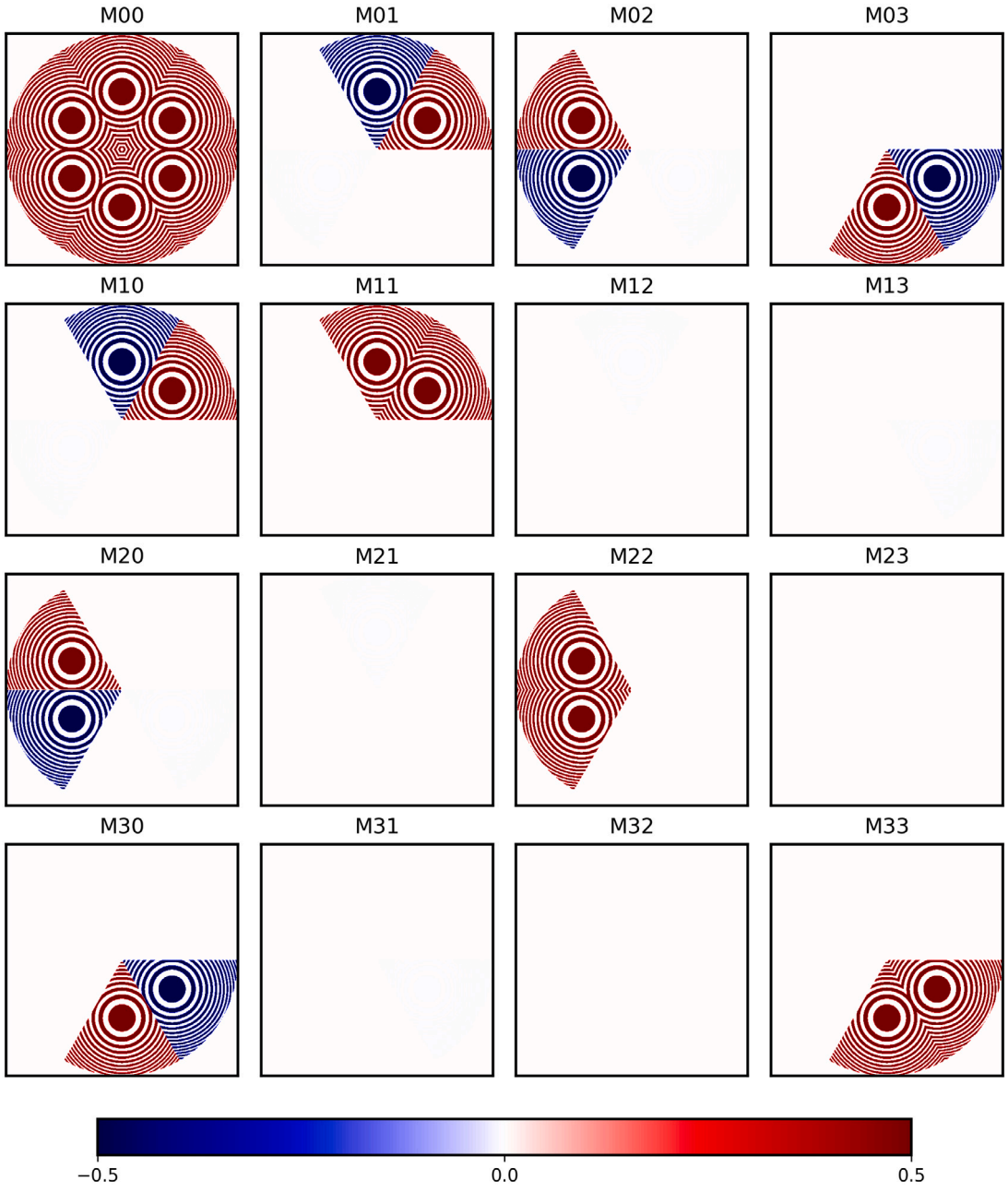

Fig. 2. Maps of the 16 elements of the 4 × 4 Mueller matrix of the proposed VDOE.

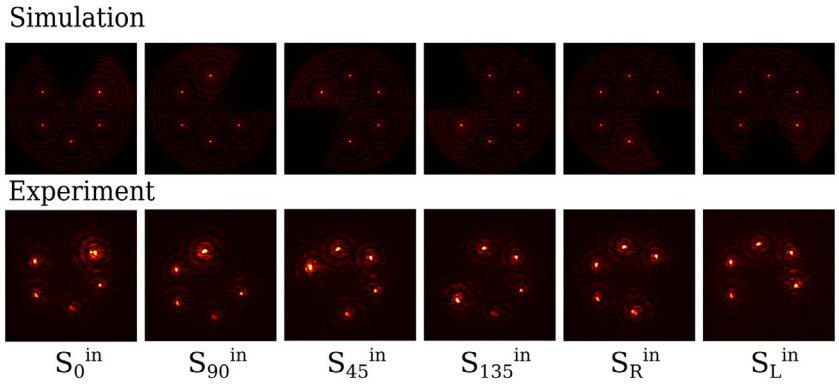

Fig. 3. Image of the intensity distributions at the focal plane of the VDOE for plane waves with the polarization states given in Table 2: simulations (upper row) and experimental results (lower row).

Table 3
Normalized and corrected Stokes vector for the ideal case and for the non-ideal case (including the diffraction cross-talk). The normalized and corrected Stokes vectors, $\vec{s}$, computed with the algorithm presented in Section 2, and error $u_0(S)$ computed using Eq. (16). Normalized and corrected Stokes vectors, $\vec{s}^{C1}$, after compensating diffractive cross-talking, and error $u_1(S)$. Normalized and corrected Stokes vectors, $\vec{s}^{C2}$, after removing systematic errors, and $u_2(S)$.

l	1	2	3	4	5	6
Input	$\vec{S}^{in}_{0°}$	$\vec{S}^{in}_{90°}$	$\vec{S}^{in}_{45°}$	$\vec{S}^{in}_{135°}$	$\vec{S}^{in}_{R}$	$\vec{S}^{in}_{L}$
$\vec{s}$	$\begin{pmatrix}1\\+0.989\\-0.004\\-0.004\end{pmatrix}$	$\begin{pmatrix}1\\-0.989\\+0.004\\+0.004\end{pmatrix}$	$\begin{pmatrix}1\\-0.004\\+0.989\\-0.004\end{pmatrix}$	$\begin{pmatrix}1\\+0.004\\-0.989\\+0.004\end{pmatrix}$	$\begin{pmatrix}1\\-0.004\\-0.004\\+0.989\end{pmatrix}$	$\begin{pmatrix}1\\+0.004\\+0.004\\-0.989\end{pmatrix}$
$u_0(S)$	0.88%	0.88%	0.91%	0.91%	0.88%	0.88%
$\vec{s}^{C1}$	$\begin{pmatrix}1\\+0.999\\-0.003\\-0.003\end{pmatrix}$	$\begin{pmatrix}1\\-0.999\\+0.003\\+0.003\end{pmatrix}$	$\begin{pmatrix}1\\-0.003\\+0.999\\-0.003\end{pmatrix}$	$\begin{pmatrix}1\\+0.003\\-0.999\\+0.003\end{pmatrix}$	$\begin{pmatrix}1\\-0.003\\-0.003\\+0.999\end{pmatrix}$	$\begin{pmatrix}1\\+0.003\\+0.003\\-0.999\end{pmatrix}$
$u_1(S)$	0.28%	0.31%	0.30%	0.30%	0.31%	0.28%
$\vec{s}^{C2}$	$\begin{pmatrix}1\\+1.000\\0.000\\0.000\end{pmatrix}$	$\begin{pmatrix}1\\-1.000\\0.000\\0.000\end{pmatrix}$	$\begin{pmatrix}1\\0.000\\+1.000\\0.000\end{pmatrix}$	$\begin{pmatrix}1\\0.000\\-1.000\\0.000\end{pmatrix}$	$\begin{pmatrix}1\\0.000\\0.000\\+1.000\end{pmatrix}$	$\begin{pmatrix}1\\0.000\\0.000\\-1.000\end{pmatrix}$
$u_2(S)$	0.012%	0.012%	0.006%	0.006%	0.006%	0.006%

In polarimetry, to properly compare two different light states, it is common to use normalized Stokes vectors, $\hat{S}$. The first component is $\hat{S}_0 = 1$, and the rest of them are normalized to S_0: $\hat{S}_j = S_j/S_0$ for $j = 1, \ldots, 3$. On the other hand, any physically realizable Stokes vector must obey the relation [36]

$$S_0 \geq \sqrt{S_1^2 + S_2^2 + S_3^2}. \tag{14}$$

Then, when a Stokes vector does not fulfill this condition, it is corrected as

$$\vec{s} = \begin{pmatrix} s_0 \\ s_1 \\ s_2 \\ s_3 \end{pmatrix} = \begin{pmatrix} 1 \\ \hat{S}_1/\alpha \\ \hat{S}_2/\alpha \\ \hat{S}_3/\alpha \end{pmatrix}, \tag{15}$$

where $\alpha = \sqrt{\hat{S}_1^2 + \hat{S}_2^2 + \hat{S}_3^2}$. In the analysis of the VDOE, we will use the normalized and corrected Stokes vector, $\vec{s}$, given in Eq. (15) to better compare Stokes vector and evaluate uncertainties and errors. This correction is especially relevant for totally polarized beams, as experimental error easily produces a non-physical Stokes parameter.

3. Performance of VDOE

After the mathematical description of the device, we analyze the performance of the device when non-ideal elements are used, and how the cross-talking between sectors caused by diffraction should be included. This analysis allows to correct systematic errors and evaluate the uncertainties for actual devices.

To check the VDOE behavior, we have used the polarization states of Table 2 and applied Eq. (12) to obtain the normalized and corrected Stokes parameter $\vec{s}$ (see Eq. (15)). We have numerically realized the 6-sector VDOE presented in Section 2 as a vector mask of 1024×1024 elements. This mask is illuminated with a plane wave with $\lambda = 0.6328$ μm. Then, we have simulated the photodetectors by placing circular total absorbers with a diameter $D = 250\,\mu$m centered at the 6 focii. The resulting Stokes vectors, given in Table 3, are very similar to the input polarization states. To analyze the differences between the Stokes parameters, $\vec{s}$, – obtained from the intensities distributions of Fig. 3 – and those of the incident beam $\vec{S}^{in}$, we have computed the distance between both Stokes vectors, which is defined as

$$u(S) = \frac{\sqrt{\sum_{j=0}^{3}\left(s_j - S_j^{in}\right)^2}}{\left|\vec{S}\right|} = \frac{\sqrt{\sum_{j=0}^{3}\Delta S_j^2}}{\left|\vec{S}\right|} \tag{16}$$

where $\left|\vec{S}\right|$ corresponds to the calculated Stokes vector module. The values of this uncertainty, $u_0(S)$, for these examples are included in Table 3. They range between 0.88% and 0.91%. Although these uncertainties are small, they are not negligible and deserve further analysis.

3.1. Diffractive effects and normalization

The focusing capabilities of each sector is one of the reasons behind these uncertainties. Ideally, all the light traveling through sector k, should focus on the corresponding detector. However, the diffractive effects of the VDOE scatter a fraction of that light towards other detectors. This cross-talking effect is larger when the null state differs from the perfect absorber condition, and also when the size of the sectors is smaller or the number of sectors increases. The combination of these effects increases the uncertainty in the computation of the Stokes vector. To reduce this uncertainty, the contribution of the spurious light can be evaluated by sequentially illuminating each sector k while blocking the rest of them. The illuminating beam must be totally depolarized or be the state of highest transmission of each sector (the states shown in Table 2 for our VDOE described previously, considering $l = k$). Then, for this selective illumination at each sector k, the intensity at every detector $k' = 1, 2, \ldots, N$ is measured. These intensities are arranged as a $N \times N$ matrix, where the element $D_{k'k}$ represents the intensity received by detector k' when only sector k is illuminated. For our 6-sector VDOE presented in Section 2, the matrix we calculated is

$$\boldsymbol{D} = \begin{pmatrix} 1.0000 & 0.0033 & 0.0005 & 0.0004 & 0.0005 & 0.0033 \\ 0.0033 & 1.0000 & 0.0033 & 0.0005 & 0.0004 & 0.0005 \\ 0.0005 & 0.0033 & 1.0000 & 0.0033 & 0.0005 & 0.0004 \\ 0.0004 & 0.0005 & 0.0033 & 1.0000 & 0.0033 & 0.0005 \\ 0.0005 & 0.0004 & 0.0005 & 0.0033 & 1.0000 & 0.0033 \\ 0.0033 & 0.0005 & 0.0004 & 0.0005 & 0.0033 & 1.0000 \end{pmatrix}. \tag{17}$$

To generate a first-order correction, we multiply the intensity vector by D^{-1},

$$\vec{I}^{C1} = \boldsymbol{D}^{-1}\vec{I}. \tag{18}$$

Finally, we use I_m^{C1} in Eq. (9) instead of I_m. After the correction of the diffractive cross-talking, we can re-generate an improved evaluation of the Stokes parameters $\vec{s}^{C1}$ that is presented in Table 3. The maximum uncertainty in the Stokes vectors, $u_1(S)$, is reduced from 0.91% to 0.31% (see Table 3).

For simulations, the intensities do not need to be normalized to the maximum value from all sectors because we can assume that the intensity is evenly distributed on the aperture of the VDOE. However,

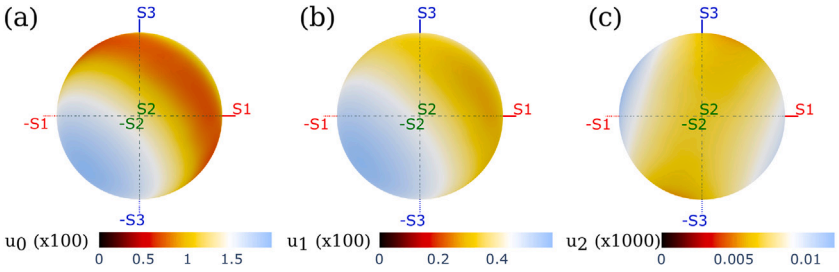

Fig. 4. Total uncertainty for pure polarization states when (a) diffractive effects are not corrected, $u_0(\boldsymbol{S})$ (see Eq. (16)), (b) diffractive effects are corrected using Eq. (18), $u_1(\boldsymbol{S})$, and (c) systematic errors are removed using Eq. (21), $u_2(\boldsymbol{S})$. This description using the Poincaré sphere is equivalent to a map in terms of azimuth and ellipticity angle of the polarized light since the other side of the spheres is symmetrical to the front face.

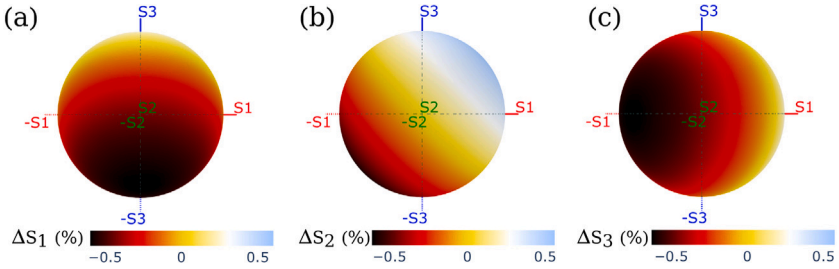

Fig. 5. Differences ΔS_1, ΔS_2, and ΔS_3, between the computed Stokes parameters $\vec{s}^{\,\mathrm{sim,C1}}$ and the input Stokes parameters.

it is a very important procedure for experiments since it considers any variability in design: differences in areas between sectors, a different transmissivity or efficiency of the detectors, or a non-homogeneous illumination over the sectors. In this last case, a normalization matrix $\boldsymbol{N}$ must be used to correct the intensities. In contrast to simulations, where $\boldsymbol{N}$ is the identity matrix, in the experiment the normalization matrix will depend on the singular characteristics of the manufactured VDOE and the light source used. This compensation of diffractive and normalization effects only needs to be done once during the device calibration process. However, if the irradiance distribution of the beam is not homogeneous, this procedure should be repeated for each inhomogeneous beam irradiance.

3.2. Systematic uncertainty

To better understand the behavior of the uncertainty, instead of limiting our analysis to the states selected in Table 2, we have computed $u_0(S)$ and $u_1(S)$ for a collection of 250 states that samples the Poincaré sphere regularly. We have used the Fibonacci sphere algorithm to determine the selected states of polarization on the sphere [40]. In Fig. 4.a, we can see the computed uncertainty at the Poincaré sphere by using Eq. (9), u_0. In Fig. 4.b, we have also removed diffractive effects by using Eq. (18) to obtain u_1. From these two figures, we can observe that the uncertainties vary smoothly and represent systematic errors mostly caused by the pixel size of the VDOE, that affects the faithful reproduction of the outer zones of the FZPs. In fact, we have checked that increasing resolution decreases the error. Then, due to limitations in resolution of our experimental set-up, we should expect larger errors and uncertainties for our fabricated device. Therefore, this first order correction $u_1(S)$ can compensate diffractive effects improving the performance of the proposed devices. To refine the analysis, it is possible to obtain the uncertainties for each component ΔS_1, ΔS_2, and ΔS_3, which are shown in Fig. 5a–c, respectively.

Since the differences in the simulations, Fig. 5, vary in a very uniform matter for each component, they can be fitted to a linear dependence of the different components,

$$\Delta S_j \approx a_j + b_j S_1 + c_j S_2 + d_j S_3, \tag{19}$$

and we have obtained the following values

$$\begin{aligned} \Delta S_1 &= +0.0003 - 0.0002\, S_1 + 0.0030\, S_2 + 0.0030\, S_3, \\ \Delta S_2 &= +0.0000 + 0.0030\, S_1 + 0.0002\, S_2 + 0.0030\, S_3, \\ \Delta S_3 &= -0.0002 + 0.0030\, S_1 + 0.0030\, S_2 - 0.0002\, S_3. \end{aligned} \tag{20}$$

As a consequence, most of the error found in Fig. 4 is systematic and can be corrected using

$$\vec{S}^{C2} = \vec{S}^{C1} - \Delta\vec{S}, \tag{21}$$

where $\Delta\vec{S} = \begin{bmatrix} 0, & \Delta S_1, & \Delta S_2, & \Delta S_3 \end{bmatrix}^T$. With this new correction, the uncertainty in the estimation of the Stokes parameters, $u_2(S)$ presents a maximum of 0.012% with an averaged value of 0.006% (see Fig. 4.c). In Table 3, we present the uncertainties for the six original states of polarizations considered in Section 2, where we can see how the system retrieves the input Stokes vector with high fidelity.

4. Experimental results

To validate the proposed design, we have experimentally verified its polarization characterization capabilities of the VDOE by realizing and testing a working device. The set-up is shown in Fig. 6. The light source is a linearly polarized He-Ne laser ($\lambda = 0.6328$ μm) with a Gaussian beam profile. A spatial filter, formed by a 40× microscope objective, a 10 μm pinhole, and a collimating lens, is used to expand the beam and to completely illuminate the VDOE as evenly as possible. A polarizer (P) and a quarter-waveplate (QW) are used to obtain circular polarization. In addition, a motorized rotating polarizer (R-P) and a motorized rotating quarter-waveplate (R-QW) are used to generate an arbitrary totally polarized state [41].

For better comparison to simulations, we fabricated a sectorized VDOE with $N = 6$ sectors. It is formed by a superposition of an amplitude mask – with opaque zones printed on a transparent substrate – and a vector mask formed by 6 polarizers and 2 quarter-waveplates (these quarter-waveplates are combined with linear polarizers for two of the sectors) which are manually aligned and individually shaped to reproduce the sectors presented in Section 2 and shown in Figs. 1 and 2. The diameter of the clear aperture of the VDOE is $D = 29$ mm, and

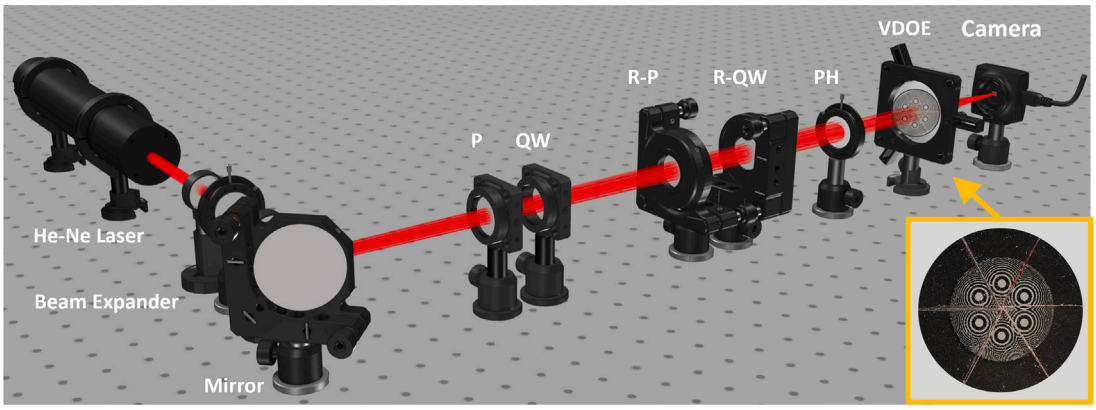

Fig. 6. Graphical representation of the experimental set-up. We use a He-Ne laser and a beam expander to generate a collimated light beam. Then, circular polarized light is produced with a polarizer (P) and a quarter-waveplate (QW). We further polarize the light beam to the desired value with a motorized rotating polarizer and quarter-waveplate (R-P and R-QW, respectively). Afterwards, the light beam is spatially filtered through a pinhole (PH) and illuminates the VDOE fully as evenly as possible. The detection system consists of a camera to capture the intensity. On the lower right corner, we show a photograph of the manufactured VDOE.

the focal length is $f' = 550$ mm. The displacement of the optical axis of the individual FZP with respect the center of the VDOE is $\Delta r = 3.7$ mm. The plates we have used are polyvinyl alcohol-iodine polarizers and poly-carbonate quarter-waveplates (Alight and Edmund, respectively). In this experimental realization of the 6-sector VDOE, instead of using circular polarizers, the elements in sectors 5 and 6, $\boldsymbol{J}_5^{\exp}$ and $\boldsymbol{J}_6^{\exp}$, are a combination of a quarter-waveplate and a polarizer with a relative orientation of ±45°, respectively. In this way, the output polarization of the combined system will be linear, not circular, as it was described in Table 1. However, its intensity transmission is the same as the equivalent circular polarizer.

Since our polarization elements are not ideal, we have experimentally measured the Mueller matrix for each sector with a polarimeter [42], and the transmission of the null state with a power meter. The results are shown in Table 4 and can be compared to the ideal case presented in Table 1. We calculated the Jones matrices from the Mueller matrices (ignoring their depolarization properties, which were negligible) by using the polar decomposition theorem [36]. This comparison shows that null elements in the ideal case are not longer zero for the components used in the experiment, most ones are substituted by values below unity, and most of the Jones matrix elements have both real and imaginary parts.

At the focal plane of the VDOE, we place a 72BUC02-ML CMOS camera (Imaging source) with 2592 × 1944 pixels and a pixel size of 2.2×2.2 μm^2. An example of the images obtained for the six polarization states defined in Table 2 is shown in Fig. 3 (lower row). We can see that each image has five bright spots (versus 6 focii) because the sixth one corresponds to the sector which blocks the polarization state of the incident light beam. The photodetectors in charge of collecting the intensity distribution at the focii of the VDOE, I_k, have been simulated by integrating the signal on 6 circular areas with size $d = 0.2$ mm and centered at each focal point. Using these six intensities, we calculate the Stokes vectors for each of these six configurations with Eq. (12) where $\mathbf{W}^I$ is

$$\boldsymbol{W}_{\exp}^{I} = \begin{pmatrix} 0.3724 & 0.4782 & 0.5325 & 0.3676 & 0.319 & 0.3753 \\ 1.1031 & -1.2353 & -0.0966 & 0.1823 & 0.0392 & 0.0509 \\ 0.1269 & 0.2334 & 1.206 & -1.0306 & -0.0219 & -0.0248 \\ -0.0643 & -0.0944 & 0.1253 & -0.0358 & 1.3928 & -1.521 \end{pmatrix}. \tag{22}$$

Using Eq. (15) instead of Eq. (9) is particularly important for sectors 5 and 6, with which S_3 is evaluated. This happens because they have both polarizers and retarders plates, and the precise angular adjustment of the elements is not perfect for the experimental realization of the device. Also, since the beam does not fill the VDOE aperture homogeneously, the normalization correction (Eq. (24)) described in Section 3.1 is necessary as well as the diffraction correction (Eq. (25)). Therefore, the corrected intensities are obtained as

$$\vec{I}' = \boldsymbol{D}_{\exp}^{-1}\boldsymbol{N}_{\exp}^{-1}\vec{I}, \tag{23}$$

where

$$\boldsymbol{N}_{\exp} = \begin{pmatrix} 0.909 & 0 & 0 & 0 & 0 & 0 \\ 0 & 1 & 0 & 0 & 0 & 0 \\ 0 & 0 & 0.771 & 0 & 0 & 0 \\ 0 & 0 & 0 & 0.915 & 0 & 0 \\ 0 & 0 & 0 & 0 & 0.585 & 0 \\ 0 & 0 & 0 & 0 & 0 & 0.681 \end{pmatrix}, \tag{24}$$

and

$$\boldsymbol{D}_{\exp} = \begin{pmatrix} 1 & 0.0124 & 0.0072 & 0.0019 & 0.0187 & 0.0268 \\ 0.0070 & 1 & 0.0103 & 0.0159 & 0.0122 & 0.0031 \\ 0.015 & 0.0019 & 1 & 0.0089 & 0.0144 & 0.0008 \\ 00024. & 0.0291 & 0.0290 & 1 & 0.0082 & 0.0017 \\ 0.0030 & 0.0012 & 0.1430 & 0.0014 & 1 & 0.0051 \\ 0.0172 & 0.0019 & 0.0103 & 0.0012 & 0.1940 & 1 \end{pmatrix}. \tag{25}$$

Besides, we have generated 400 polarization states distributed on the Poincaré sphere to experimentally mimic the simulated case. Then, we subtract the experimental systematic errors, as shown in Section 3.2. However, in this case, to improve the results, we have performed a quadratic fitting instead of a linear one (see Fig. 7),

$$\Delta S_j \approx a_j + b_j S_1 + c_j S_2 + d_j S_3 + e_j S_1^2 + f_j S_2^2 + g_j S_3^2, \qquad \text{where} \quad j = 1, 2, 3. \tag{26}$$

After applying all these corrections, the experimental error reduces significantly. In Table 5, we summarize the experimental Stokes vectors with their respective errors for the six polarization states associated to the six sectors of the VDOE. These errors range between 0.39% and 4.99%, with an uncertainty average of 2.20%. Finally, we have analyzed the Stokes vectors over the whole Poincaré sphere (for 400 incident polarization states) and we have determined the error for each one (see Fig. 8.a). The mean and maximum errors are 3.33% and 6.97%, respectively.

To validate the device and analyze the sources of uncertainty, we repeated the experiment substituting the fabricated VDOE by a motorized quarter-waveplate and polarizer to simulate the six VDOE sectors, performing the six intensity measurements sequentially. We also substituted the camera with a photodiode. Then, for each incident state, we rotated the analyzer optics so their Mueller matrix would correspond to the ones in Table 4. As in the previous experiment, we repeated it for the same 400 input states. The uncertainty of the

Table 4
Experimental Jones and Mueller matrices for the fabricated VDOE. We have obtained the Jones matrices from the decomposition of Mueller matrices as the combination of a pure polarizer and a retarder. Also, in this calculation, we have disregarded depolarization effects.

Index	Name	Jones matrix	Mueller matrix
0	$\boldsymbol{J}_0^{\exp}$	$\begin{pmatrix} 0.2383 & 0 \\ 0 & 0.2383 \end{pmatrix}$	$\begin{pmatrix} 0.056 & 0 & 0 & 0 \\ 0 & 0.056 & 0 & 0 \\ 0 & 0 & 0.056 & 0 \\ 0 & 0 & 0 & 0.056 \end{pmatrix}$
1	$\boldsymbol{J}_1^{\exp}$	$\begin{pmatrix} 0.912 & -0.002-0.006i \\ -0.017+0.027i & 0.005-0.011i \end{pmatrix}$	$\begin{pmatrix} 0.416 & 0.416 & -0.001 & 0.012 \\ 0.415 & 0.415 & -0.008 & 0.016 \\ -0.017 & -0.019 & 0.003 & -0.008 \\ 0.026 & 0.032 & -0.001 & 0.000 \end{pmatrix}$
2	$\boldsymbol{J}_2^{\exp}$	$\begin{pmatrix} 0.029 & -0.115-0.032i \\ -0.104+0.023i & 0.908-0.089i \end{pmatrix}$	$\begin{pmatrix} 0.430 & -0.417 & -0.101 & 0.009 \\ -0.414 & 0.404 & 0.096 & -0.007 \\ -0.113 & 0.111 & 0.018 & 0.002 \\ 0.007 & -0.007 & -0.004 & 0.001 \end{pmatrix}$
3	$\boldsymbol{J}_3^{\exp}$	$\begin{pmatrix} 0.423 & 0.455-0.016i \\ 0.474+0.039i & 0.508+0.055i \end{pmatrix}$	$\begin{pmatrix} 0.437 & -0.032 & 0.436 & 0.016 \\ -0.050 & +0.003 & -0.061 & -0.003 \\ 0.433 & -0.055 & 0.429 & 0.015 \\ 0.035 & -0.004 & 0.032 & 0.001 \end{pmatrix}$
4	$\boldsymbol{J}_4^{\exp}$	$\begin{pmatrix} 0.573 & -0.453-0.012i \\ -0.478+0.024i & 0.368-0.038i \end{pmatrix}$	$\begin{pmatrix} 0.450 & 0.107 & -0.436 & 0.020 \\ 0.083 & 0.015 & -0.079 & -0.006 \\ -0.441 & -0.101 & 0.431 & -0.021 \\ 0.028 & -0.001 & -0.024 & 0.003 \end{pmatrix}$
5	$\boldsymbol{J}_5^{\exp}$	$\begin{pmatrix} 0.632 & -0.097-0.53i \\ -0.041-0.066i & -0.04-0.061i \end{pmatrix}$	$\begin{pmatrix} 0.345 & 0.060 & -0.057 & 0.335 \\ 0.344 & 0.049 & -0.067 & 0.345 \\ -0.012 & -0.002 & 0.008 & -0.013 \\ -0.018 & -0.005 & 0.003 & -0.014 \end{pmatrix}$
6	$\boldsymbol{J}_6^{\exp}$	$\begin{pmatrix} 0.588 & -0.02+0.595i \\ -0.065+0.083i & -0.035+0.099i \end{pmatrix}$	$\begin{pmatrix} 0.350 & 0.007 & -0.012 & -0.350 \\ 0.350 & -0.015 & -0.011 & -0.350 \\ -0.009 & 0.000 & 0.000 & 0.018 \\ 0.005 & 0.007 & -0.001 & -0.003 \end{pmatrix}$

Table 5
Experimentally generated ($\vec{S}_g^{\exp}$) and measured ($\vec{S}_a^{\exp}$) Stokes vectors, and uncertainties $u_2^{\exp}(S)$ computed using Eq. (16).

Index	1	2	3	4	5	6
Input	$\vec{S}_{0°}^{\text{in}}$	$\vec{S}_{90°}^{\text{in}}$	$\vec{S}_{45°}^{\text{in}}$	$\vec{S}_{135°}^{\text{in}}$	$\vec{S}_R^{\text{in}}$	$\vec{S}_L^{\text{in}}$
$\vec{S}_g^{\exp}$	$\begin{pmatrix} 1 \\ 0.997 \\ 0 \\ -0.083 \end{pmatrix}$	$\begin{pmatrix} 1 \\ -0.984 \\ -0.160 \\ 0.083 \end{pmatrix}$	$\begin{pmatrix} 1 \\ -0.08 \\ 0.993 \\ 0.083 \end{pmatrix}$	$\begin{pmatrix} 1 \\ -0.087 \\ -0.993 \\ 0.083 \end{pmatrix}$	$\begin{pmatrix} 1 \\ 0 \\ 0 \\ 1 \end{pmatrix}$	$\begin{pmatrix} 1 \\ 0 \\ 0 \\ -1 \end{pmatrix}$
$\vec{S}_a^{\exp}$	$\begin{pmatrix} 1 \\ 0.993 \\ -0.062 \\ -0.098 \end{pmatrix}$	$\begin{pmatrix} 1 \\ -0.985 \\ -0.156 \\ 0.079 \end{pmatrix}$	$\begin{pmatrix} 1 \\ -0.084 \\ 0.989 \\ 0.082 \end{pmatrix}$	$\begin{pmatrix} 1 \\ -0.099 \\ -0.995 \\ 0.013 \end{pmatrix}$	$\begin{pmatrix} 1 \\ 0.021 \\ -0.001 \\ 1 \end{pmatrix}$	$\begin{pmatrix} 1 \\ -0.014 \\ 0.007 \\ -1 \end{pmatrix}$
$u_2^{\exp}(S)$	4.55%	0.45%	0.39%	4.99%	1.48%	1.10%

measured Stokes vectors, u^{seq}, is shown in Fig. 8.b. The maximum discrepancy is 2.76% and the average uncertainty is 1.47%. This proves that our experimental set-up (without VDOE) already generates a non-negligible error due to the uncertainty in the angles of the optical elements and being them non-ideal. These numbers show that the mean uncertainties in the measurements of the VDOE is about twice the value obtained for the sequential measurement. We believe that this difference in the uncertainty is caused by fabrication defects and the uncertainty in the characterization of the polarizing elements of the VDOE.

5. Conclusions

In this contribution, we exploit the extended capabilities of VDOEs to propose and demonstrate a polarization analyzer that allows the simultaneous evaluation of the four Stokes parameters of an incoming beam. The aperture of the device is sectorized angularly in six portions. The VDOE is based on six FZP that are laterally displaced to allow a spatial separation of their corresponding focii. Each FZP fills one angular sector and is combined with the appropriate arrangement of polarization elements: linear polarizers and quarter-waveplates. The light reaching each sector is focused and its intensity depends on the polarimetric properties of the incident light beam and the polarization components associated to each sector. Using these signals, we have proposed a procedure to obtain the Stokes parameter with our VDOE.

Our numerical simulations show that, due to diffractive effects, light from one sector can leak into other sectors, significantly increasing the error in the measurement. To improve the accuracy of the device, we removed these cross-talking effects by sequentially illuminating each sector and retrieving the signal from the photodetectors. This information is included in a correction matrix that takes into account this effect. Moreover, we performed a detailed analysis of the uncertainties of the individual components of the Stokes vector which revealed a systematic error where each component shows a dependence with respect to the others. This analysis has been done for a collection of 250 polarization states regularly spaced on the Poincaré sphere. Once characterized, this error has been corrected by a linear or quadratic fitting, depending on the distribution of the discrepancies. Our simulations show how the uncertainties can be reduced to a maximum value of 0.012%, with an averaged value of 0.006%. To experimentally evaluate the performance of the design, we have fabricated a VDOE device using real (non-ideal) FZP and polarization elements. The Mueller matrices of these elements

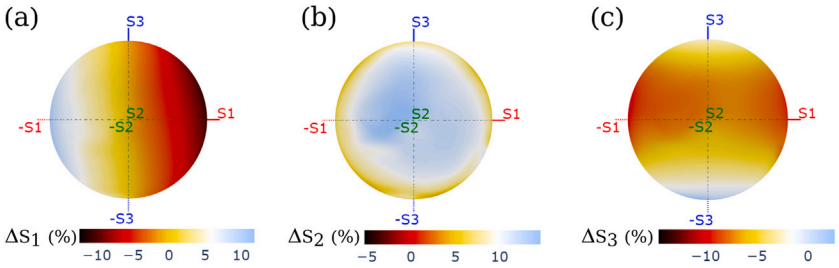

Fig. 7. Poincaré spheres with the experimental differences ΔS_1, ΔS_2, and ΔS_3, between the analyzed Stokes parameters and the input Stokes parameters.

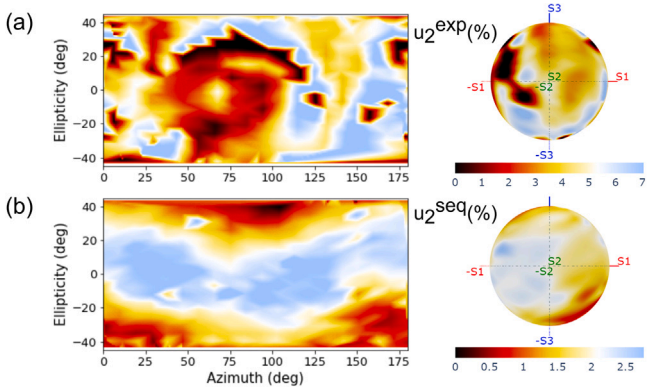

Fig. 8. Total uncertainty of Stokes vectors doing the experiment (a) with VDOE, and (b) with sequential measurements. In both situations, the azimuth-ellipticity angle maps, and the Poincaré sphere representations are complementary.

have been experimentally characterized considering the deviation from the ideal behavior. Our analysis shows that the experimental device behaves as expected and it reproduces well the components of the Stokes parameter of the incoming beam. However, it shows a larger value of the uncertainty when compared with the simulated results, with an averaged uncertainty of 3.33%. This uncertainty is mostly caused by cumulative contributions from the spatial resolution of the fabricated device and the detection mechanism, the departure from the nominal orientation of the polarization elements, and the inhomogeneity of the intensity distribution of the light beam on the aperture.

In summary, we have validated how a VDOE may help design and fabricate advanced devices by taking advantage of its design flexibility and compactness. Our design corresponds with a division-of-amplitude method that determines the Stokes vector of a light beam in real time. Instead of using successive beam splitters, it is based on a simple diffractive element sectorized in several Fresnel zone plates that have been complemented with polarizing elements. This arrangement makes possible the simultaneous measurement of the Stokes parameters without any moving parts. Therefore, the time response is only limited by the detection technique associated with each focal spot. For comparison, we have tested our device in sequential mode, obtaining, as expected, a much longer duration of the experiment with respect to the non-sequential measurement. Besides, the footprint of the device is very little and, without auxiliary optics, it is axially determined by the focal length of the VDOE. Altogether, this makes our design reliable, compact, and cheap.

CRediT authorship contribution statement

Angela Soria-Garcia: Conceptualization, Methodology, Software, Validation, Formal analysis, Investigation, Data curation, Writing. **Jesus del Hoyo:** Conceptualization, Methodology, Software, Validation, Formal analysis, Investigation, Data curation, Writing, Supervision. **Luis Miguel Sanchez-Brea:** Conceptualization, Methodology, Software, Validation, Formal analysis, Investigation, Data curation, Writing, Supervision, Project administration, Funding acquisition. **Veronica Pastor-Villarrubia:** Validation, Investigation, Writing – review & editing. **Veronica Gonzalez-Fernandez:** Validation, Investigation, Writing – review & editing. **Mahmoud H. Elshorbagy:** Investigation, Writing – review & editing. **Javier Alda:** Conceptualization, Methodology, Validation, Investigation, Formal analysis, Writing, Supervision, Project administration, Funding acquisition.

Acknowledgments

Authors acknowledge funding from Retos Colaboración 2019 "Teluro" project RTC2019-007113-3, Ministerio de Economía *y* Competitividad, Spain and the European Union, European funds for regional development; and from Plan Nacional de Investigación from Ministerio de Ciencia e Innovación, Spain "Nanorooms" project PID2019-105918GB-I00. The authors also thank to Dr. Irene Alda for her help with the English style and grammar in the final edition of this contribution.

References

[1] Q.H. Phan, Y.L. Lo, Stokes-Mueller matrix polarimetry system for glucose sensing, Opt. Lasers Eng. 92 (2017) 120–128, http://dx.doi.org/10.1016/j.optlaseng.2016.08.017.

[2] D.H. Goldstein, Polarized Light, CRC Press, 2017.

[3] R.A. Chipman, W.S.T. Lam, G. Young, Polarized Light and Optical Systems, Optical Sciences and Applications of Light, CRC Press, 2018, http://dx.doi.org/10.1201/9781351129121.

[4] R.M.A. Azzam, Stokes-vector and Mueller-matrix polarimetry, J. Opt. Soc. Amer. A 33 (7) (2016) 1396–1408.

[5] P.A. Williams, Rotating-wave-plate Stokes polarimeter for differential group delay measurements of polarization-mode dispersion, Appl. Opt. 38 (31) (1999) 6508–6515.

[6] D.S. Sabatke, M.R. Descour, E.L. Dereniak, W.C. Sweatt, S.A. Kemme, G.S. Phipps, Optimization of retardance for a complete Stokes polarimeter, Opt. Lett. 25 (11) (2000) 802–804.

[7] J. Kaneshiro, T.M. Watanabe, H. Fujita, T. Ichimura, Full control of polarization state with a pair of electro-optic modulators for polarization-resolved optical microscopy, Appl. Opt. 55 (5) (2016) 1082–1089.

[8] J.M. Bueno, Polarimetry using liquid-crystal variable retarders: Theory and calibration, J. Opt. A: Pure Appl. Opt. 2 (3) (2000) 216.

[9] A.J. Hunt, D.R. Huffman, A new polarization-modulated light scattering instrument, Rev. Sci. Instrum. 44 (12) (1973) 1753–1762.

[10] R.M.A. Azzam, Division-of-amplitude photopolarimeter (DOAP) for the simultaneous measurement of all four Stokes parameters of light, Optica Acta: Int. J. Opt. 29 (5) (1982) 685–689.

[11] T. Todorov, L. Nikolova, Spectrophotopolarimeter: Fast simultaneous real-time measurement of light parameters, Opt. Lett. 17 (5) (1992) 358–359.

[12] Y. Cui, R.M.A. Azzam, Sixteen-beam grating-based division-of-amplitude photopolarimeter, Opt. Lett. 21 (1) (1996) 89–91, http://dx.doi.org/10.1364/OL.21.000089, URL https://opg.optica.org/ol/abstract.cfm?URI=ol-21-1-89.

[13] J. Alda, G. Boreman, Infrared Antennas and Resoant Structures, SPIE Press, 2017, http://dx.doi.org/10.1117/3.2282288, URL https://spie.org/Publications/Book/2282290?SSO=1.

[14] E. Briones, A. Cuadrado, J. Briones, R.D. de León, J.C. Martínez-Antón, S. McMurtry, M. Hehn, F. Montaigne, J. Alda, F.J. González, Seebeck nanoantennas for the detection and characterization of infrared radiation, Opt. Express 22 (S6) (2014) A1538–A1546, http://dx.doi.org/10.1364/OE.22.0A1538, URL http://opg.optica.org/oe/abstract.cfm?URI=oe-22-106-A1538.

[15] P. Krenz, J. Alda, G. Boreman, Orthogonal infrared dipole antenna, Infrared Phys. Technol. 51 (4) (2008) 340–343, http://dx.doi.org/10.1016/j.infrared.2007.09.002, URL https://www.sciencedirect.com/science/article/pii/S1350449507000898.

[16] A. Cuadrado, E. Briones, F.J. González, J. Alda, Polarimetric pixel using seebeck nanoantennas, Opt. Express 22 (11) (2014) 13835–13845, http://dx.doi.org/10.1364/OE.22.013835, URL http://opg.optica.org/oe/abstract.cfm?URI=oe-22-11-13835.

[17] J.S. Tharp, J.M. Lopez-Alonso, J.C. Ginn, C.F. Middleton, B.A. Lail, B.A. Munk, G.D. Boreman, Demonstration of a single-layer meanderline phase retarder at infrared, Opt. Lett. 31 (18) (2006) 2687–2689, http://dx.doi.org/10.1364/OL.31.002687, URL http://opg.optica.org/ol/abstract.cfm?URI=ol-31-18-2687.

[18] J.S. Tharp, J. Alda, G.D. Boreman, Off-axis behavior of an infrared meander-line waveplate, Opt. Lett. 32 (19) (2007) 2852–2854, http://dx.doi.org/10.1364/OL.32.002852, URL http://opg.optica.org/ol/abstract.cfm?URI=ol-32-19-2852.

[19] M.H. Elshorbagy, L.M. Sanchez-Brea, J. Buencuerpo, J. del Hoyo, A. Soria-Garcia, V.P.-V. adn Alejandro San-Blas, A. Rodriguez, S.M. Olaizola, J. Alda, Polarization conversion using customized subwavelength laser-induced periodic surface structures on stainless steel, Photonics Res. (2022) http://dx.doi.org/10.1364/PR.454451.

[20] E. Arbabi, S.M. Kamali, A. Arbabi, A. Faraon, Full-stokes imaging polarimetry using dielectric metasurfaces, ACS Photonics 5 (8) (2018) 3132–3140, http://dx.doi.org/10.1021/acsphotonics.8b00362.

[21] N.A. Rubin, Z. Shi, F. Capasso, Polarization in diffractive optics and metasurfaces, Adv. Opt. Photonics 13 (4) (2021) 836, http://dx.doi.org/10.1364/aop.439986.

[22] N.A. Rubin, P. Chevalier, M. Juhl, M. Tamagnone, R. Chipman, F. Capasso, Imaging polarimetry through metasurface polarization gratings, Opt. Express 30 (6) (2022) 9389–9412, http://dx.doi.org/10.1364/OE.450941, URL http://opg.optica.org/oe/abstract.cfm?URI=oe-30-6-9389.

[23] J. Turunen, F. Wyrowski, Diffractive optics for industrial and commercial applications, 1998.

[24] D.C. O'Shea, T.J. Suleski, A.D. Kathman, D.W. Prather, Diffractive Optics: Design, Fabrication, and Test,Vol. 62, Spie Press Bellingham, WA, 2004.

[25] B.C. Kress, P. Meyrueis, Bernard C. Kress, P. Meyruei, Applied Digital Optics, From Micro-Optics to Nanophotonics, John Wiley & Sons, 2009, http://dx.doi.org/10.1002/9780470022658.

[26] H.P. Herzig, Micro-Optics: Elements, Systems and Applications, CRC Press, 2014.

[27] F.J. Torcal-milla, L.M. Sanchez-brea, A. Gomez-pedrero, Sector-based Fresnel zone plate with extended depth of focus, Opt. Laser Technol. 154 (May) (2022) 1–15, http://dx.doi.org/10.1016/j.optlastec.2022.108294.

[28] S.N. Khonina, A.V. Ustinov, S.A. Fomchenkov, A.P. Porfirev, Formation of hybrid higher-order cylindrical vector beams using binary multi-sector phase plates, Sci. Rep. 8 (1) (2018) 1–11, http://dx.doi.org/10.1038/s41598-018-32469-0.

[29] L. Janicijevic, S. Topuzoski, L. Stoyanov, A. Dreischuh, Diffraction of a Gaussian beam by a four-sector binary grating with a shift between adjacent sectors, Opt. Commun. 389 (2016) (2017) 203–211, http://dx.doi.org/10.1016/j.optcom.2016.12.041.

[30] A. Martínez, I. Moreno, M.M. Sánchez-López, Comparative analysis of time and spatially multiplexed diffractive optical elements in a ferroelectric liquid crystal display, Japan. J. Appl. Phys. 47 (3 PART 1) (2008) 1589–1594, http://dx.doi.org/10.1143/JJAP.47.1589.

[31] F.J. Salgado-Remacha, L.M. Sanchez-Brea, F.J. Alvarez-Rios, E. Bernabeu, Rough Fresnel zone plates over metallic surfaces, Appl. Opt. 49 (10) (2010) 1750–1756, http://dx.doi.org/10.1364/AO.49.001750.

[32] F.J. Torcal-Milla, L.M. Sanchez-Brea, Gaussian-Schell-model beams propagating through rough gratings, J. Opt. Soc. Amer. A 28 (3) (2011) 308, http://dx.doi.org/10.1364/josaa.28.000308.

[33] F. Javier Salgado-Remacha, F.J. Torcal-Milla, L.M. Sanchez-Brea, E. Bernabeu, Use of steel substrates in diffractive optics: Near field of high surface quality steel tape gratings, Opt. Lasers Eng. 49 (3) (2011) 356–360, http://dx.doi.org/10.1016/j.optlaseng.2010.10.009.

[34] L.M. Sanchez-Brea, F.J. Torcal-Milla, Self-imaging of gratings with two roughness levels, Opt. Commun. 285 (1) (2012) 13–17, http://dx.doi.org/10.1016/j.optcom.2011.09.017.

[35] M. Bass, Handbook of Optics. Vol 2, Devices, Measurements, and Properties, McGraw-Hill, 1995.

[36] J.J. Gil, R. Ossikovski, Polarized Light and the Mueller Matrix Approach, CRC Press, 2022.

[37] H. Ye, C.W. Qiu, K. Huang, J. Teng, B. Luk'Yanchuk, S.P. Yeo, Creation of a longitudinally polarized subwavelength hotspot with an ultra-thin planar lens: Vectorial Rayleigh-Sommerfeld method, Laser Phys. Lett. 10 (6) (2013) http://dx.doi.org/10.1088/1612-2011/10/6/065004.

[38] L.M. Sanchez-Brea, Diffratio, Python module for diffraction and interference optics, 2019, URL https://pypi.org/project/diffractio/.

[39] J. del Hoyo, L.M. Sanchez-Brea, A. Soria-Garcia, Open source library for polarimetric calculations, py_pol, in: Proceedings of SPIE, vol. 1187506, 2021, p. 3, http://dx.doi.org/10.1117/12.2597163.

[40] Y. Zhou, Arrangements of Points on the Sphere (Ph.D. thesis), 1995.

[41] J. Nicolás, J. Campos, M.J. Yzuel, Phase and amplitude modulation of elliptic polarization states by nonabsorbing anisotropic elements: Application to liquid-crystal devices, J. Opt. Soc. Amer. A 19 (5) (2002) 1013–1020.

[42] J. del Hoyo, L.M. Sanchez-Brea, J.A. Gomez-Pedrero, High precision calibration method for a four-axis Mueller matrix polarimeter, Opt. Lasers Eng. 132 (2020) http://dx.doi.org/10.1016/j.optlaseng.2020.106112.